Cross Domain Modelling of a Meander Beam MEMS Bulk Micromachined Accelerometer in COMSOL Multiphysics® and SPICE

Mahdieh Shojaei Baghini[1]
1. Department of Mechanical, Maritime and Materials Engineering, Delft University of Technology, Delft, Netherlands

Abstract: This paper presents the design of a bulk Silicon MEMS single-axis 8-beam accelerometer utilizing meander beams in the Structural Mechanics and MEMS Module of COMSOL Multiphysics®. To obtain further insights into the design of the accelerometer, an electrical lumped element model of the structure is derived and represented in SPICE. Quantities such as eigenfrequencies and proof-mass displacement have been extracted from COMSOL Multiphysics® as well as analytical studies. The effects of parasitic frequencies in the structure are observed by automatic tilting of the accelerometer at higher order eigenfrequencies due to finite off-axis stiffness coefficients. In order to mathematically quantify the response of the accelerometer arising due to parasitic frequencies, the transient damping response has been derived in COMSOL Multiphysics® as well as SPICE, and the differences are highlighted. Finally, the eigenfrequencies of the meander-beam accelerometer have been compared with that of a simple-beam accelerometer and the validity of small deflection theory is tested for the lumped model approach. While the target damping factor of the accelerometer was 0.7, the obtained damping factor increased to 1.1 due to the aforementioned parasitic frequencies and reduction in the resonance frequency of the sensor. This effect was precisely captured during the COMSOL Multiphysics® simulations.

Keywords: COMSOL Multiphysics, MEMS accelerometer, SPICE, parasitic, meander beam, eigenfrequency

1. Introduction

The development of accelerometers based on microelectromechanical (MEMS) technology has gained traction on account of their ability to be manufactured using standard clean room procedures, low power consumption, CMOS integration capabilities and microsystem reliability [1-3]. Devices utilizing capacitive [4] and piezoresistive [5] sensors are implemented in health-care, automotive and aerospace industries. Capacitive accelerometers exhibit a finite bandwidth depending on their design as well sensing environment and often consist of a proof mass which is displaced due to a finite acceleration [6].

In order to analyze the behavior of the sensor based on design and damping parameters, lumped circuit and finite element modelling are used to better characterize the system prior to fabrication. Equivalent electrical circuits of the mechanical sensor can be efficiently realized by models simulated in COMSOL providing better understanding of non-electrical phenomena through fundamental constitutive relations [6-8]. This is achieved by assigning a voltage or current source to the driving force followed by assigning of variables to the network components such that energy is conserved in both the domains.

In this work, a Silicon MEMS bulk micromachined unidirectional accelerometer with squeeze-film damping is designed and analyzed in LTspice (Analog Devices) and COMSOL Multiphysics v5.4. The gap height required during packaging for a maximally flat response is derived in LTspice and the result is coupled to the simulated sensor in COMSOL. The differences which arise in the results as characterized by the resonance frequency, damping factor, parasitic frequencies and mass displacement are highlighted. In order to reduce the vertical stiffness of the beams thereby increasing sensitivity, meander beams are utilized. A second accelerometer has been designed using rectangular beams and its response compared to that of meander beams. The designed accelerometer has the capability to be integrated with symmetric and asymmetric capacitive feedback forming a closed-loop system.

2. Sensor design

2.1 Design parameters

The accelerometer has been assigned keeping in mind the desired damping factor (ζ) of 0.707 which corresponds to no overshoots in the frequency response of the system leading to more robustness. The designated sensor is shown in Fig. 1 and is damped using plates placed at a distance equal to h_0. The thickness of the proof mass is equal to 540 μm which is considered as the thickness of the silicon wafer. The dimensions of the front-side and back-side of the proof mass are determined considering an anisotropic wet etch of the wafer across its thickness. Table 1 shows the material and geometrical properties of the MEMS sensor.

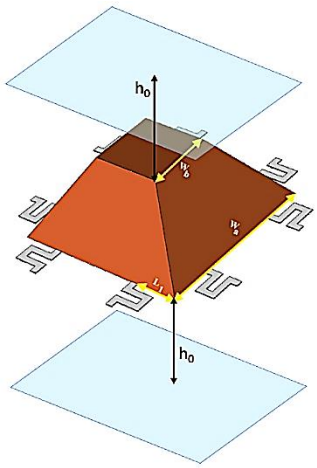

Figure 1. Bulk micromachined accelerometer with meander beams placed at a distance of L_1 from the edge.

Table 1. Material and geometrical properties of MEMS sensor.

Parameter	Value	Unit	Explanation
k_z	100	N/m	Effective beam stiffness in the vertical direction
$\Delta z/a_z$	0.1/g	$\mu m/ms^{-2}$	DC sensitivity where g is acceleration due to gravity
E	1.7×10^{11}	N/m^2	Young's modulus of Silicon
ζ	0.707	-	Damping factor
ρ	2.33×10^3	kg/m^3	Density of Silicon
η	1.98×10^{-5}	Pa sec	Viscosity of air
P_{amb}	10^5	Pa	Ambient pressure
W_a	1.25	mm	Longer width of proof mass
W_b	0.49	mm	Shorter width of proof mass

Based on the values highlighted in Table 1, the mass (M) and resonance frequency (f_0) of the structure can be derived using Eq. 1.

$$\frac{\mathbf{\Delta z}}{\mathbf{a_z}} = \frac{\mathbf{M}}{\mathbf{k_z}} = \frac{\mathbf{1}}{\mathbf{(2\pi f_0)^2}} \quad (1)$$

The mass of the structure and the resonance frequency are equal to **1.575 kHz** and **1.02 mg**, respectively.

2.2 Beam properties

The sensor has been designed such that the width of the beam (w_b) is 50 µm and the thickness of the beam (h_b) is 5 µm as shown in Fig. 2a. The effective stiffness normal to the proof mass of the beam is a function of its width, thickness, and number of beams which is equal to 8. The meander beam is a union of 5 beams as shown in Fig. 2a and the length (l_b) can be derived using Eq. 2 assuming classical beam theory.

$$\mathbf{k_z} = \frac{\mathbf{8 \cdot E \cdot w_b \cdot h_b^3}}{\mathbf{l_b}^3} \quad (2)$$

The length of each meander beam and simple beam is derived as 220 µm and 350 µm, respectively, as shown in Fig. 2a-b.

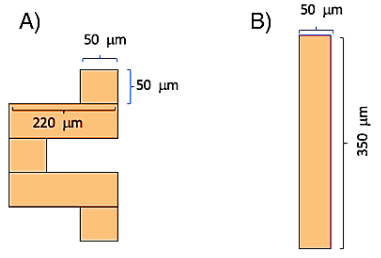

Figure 2. **a)** Meander beam constituting of 5 rectangular beams. **b)** Simple beam constituting of a single rectangular beam.

The beams have been placed at a distance of L_1 from the edge of the proof mass. In order to minimize off-axis sensitivity, L_1 should be chosen as low as possible and an initial value of 320 µm has been chosen. Lower values lead to beam collision at the edges of the mass.

3. Equivalent electrical circuit modelling

The equivalent circuit model of a squeeze film damped accelerometer is given in Fig. 3a. The force which is equal to Ma_z where a_z is the normal acceleration, is modeled by the current source **I**. Consequently, the mass is represented by the capacitor (**C** = 1.02 µF) and the compliance which is defined as the inverse of stiffness is represented by the inductor (**L** = 0.01 H). The squeeze film damping on top and bottom side of the proof mass can be designated by series RL networks connected in parallel wherein the damping component is shown by R (**R_1** and **R_2**) and the spring component is shown by L (**L_1** and **L_2**). In order to simplify the analytical derivations, the average of the top and surface area of the proof mass is considered and denoted by A_{avg}. This leads to symmetrical damping behavior of the top and bottom film and the equivalent circuit is shown in Fig. 3b. The components R_f and L_f are coupled to the mechanical domain via Eq. 3 and Eq. 4.

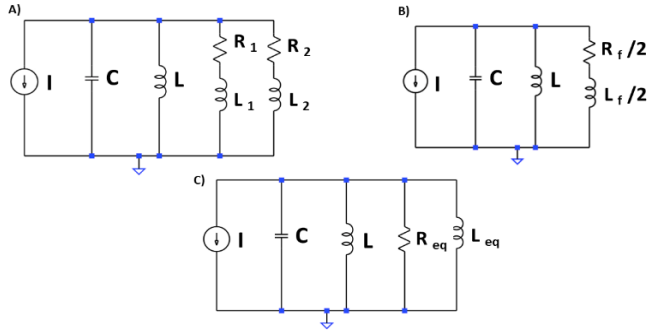

Figure 3. **a)** Electrical circuit equivalent of squeeze-film damped accelerometer. **b)** Electrical circuit considering symmetric damping. **c)** Simplified equivalent circuit for gap height derivation.

$$R_f = \frac{\pi^6 \cdot h_0^3}{384 \cdot {A_{avg}}^2 \cdot \eta} = 2 \cdot R_{damping} \quad (3)$$

$$L_f = \frac{\pi^4 \cdot h_0}{64 \cdot A_{avg} \cdot P_{amb}} = 2 \cdot L_{damping} \quad (4)$$

The transfer function of the circuit shown in Fig. 3b will be a cubic whose damping factor calculation is not straight forward. For simplifications, an equivalent parallel RL combination is derived in order to generate a transfer function which can be utilized to calculate the gap (h_0) based on the desired damping factor as shown in Fig. 3c. The inductor **L_{eq}** is equal to $L_{damping}$ and the resistor **R_{eq}** can be written as a function of the damping factor as shown in Eq. 5.

$$\zeta = \frac{1}{2 \cdot C \cdot \omega_0 \cdot R_{eq}} \quad (5)$$

Since a maximally flat frequency response is desired, ζ is set as 0.707. The values of $R_{damping}$ and $L_{damping}$ are calculated to be 70.035 Ω and 0.081 mH, respectively. Further,

$$R_f = R_{damping} \cdot \left(1 + \frac{\omega_0^2 \cdot L_{damping}^2}{R_{damping}^2}\right) \quad (6)$$

Eq. 6 is a quartic polynomial in h_0. On substituting values from Eq. 3 and Eq. 4, the desired spacing between the encapsulated mass and the plates is calculated. The solution of Eq. 6 yields an imaginary conjugate and a value in the nanometer range (this is discarded since in the nanometer range the Knudson number becomes significant and is not the case we are taking into account). The other root is the gap and is given by **h_0 = 9.66 µm**. The derived frequency response, transient response and thermomechanical noise characteristics provide further insight into the system while simultaneously aiding in the validation of our results.

Thermomechanical noise: The damper system is the primary source of noise and is thermo-mechanical by nature. The reactive components contribute as well (for example, 1/C noise generated by the capacitor), however these values are very minimal with our component values and can be ignored. The noise, $s_n(\omega)$ is analytically given by Eq. 7.

$$s_n(\omega) = \frac{4 \cdot k_B \cdot T \cdot \zeta \cdot \sqrt{M \cdot k_z}}{1 + \omega \cdot \frac{L_1}{R_1}} \quad (7)$$

The derived noise exhibits low-pass characteristics and has a value of $2.32 \cdot 10^{-22}$ A^2/Hz when computed analytically using Eq. 7. The SPICE derived noise is in excellent agreement with Eq. 7 as shown in Fig. 4.

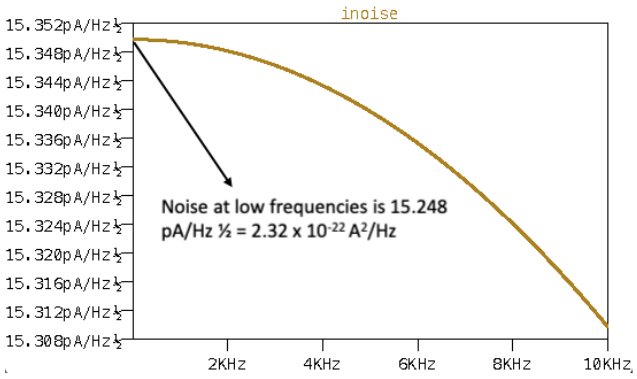

Figure 4. SPICE derived thermomechanical noise of the system.

Frequency and transient response: The validity of the derived gap required for squeeze film damping can be analyzed using the frequency and transient response. Since the accelerometer has been designed to ideally exhibit a maximally flat response (ζ = 0.707), the frequency response should show no peaking with a gain of -3dB at the resonance frequency with a phase of 90°. Further, the response of the device in the time domain exhibits one overshoot peak since the system is underdamped. The frequency and transient response are shown in Fig. 5 and Fig. 6, respectively and are in excellent agreement with the domain coupled analytical equations.

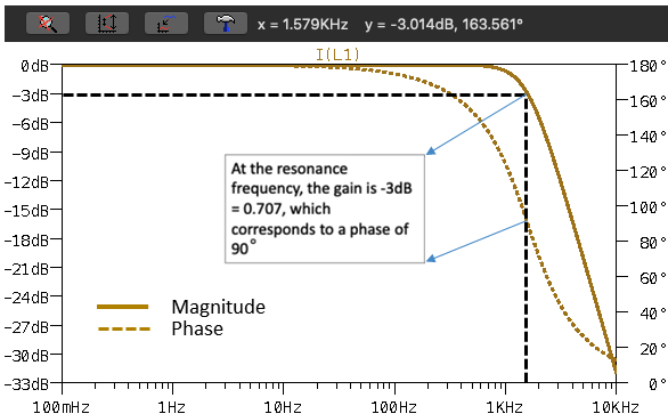

Figure 5. SPICE derived frequency response of the system. The gain is equal to -3.014 dB at a (resonance) frequency of 1.579 kHz.

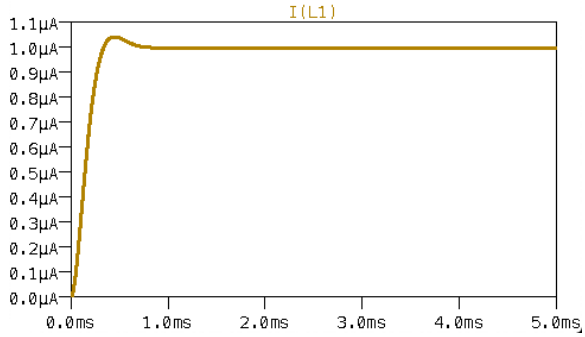

Figure 6. SPICE derived transient response of the system. An overshoot peak is present due to underdamped behavior of device.

A limitation of this method is the loss of information regarding the parasitic behavior of the accelerometer and the derivation of higher order modes. The SPICE derived gap height has been coupled with multiphysics simulations carried out in COMSOL as is discussed in section 4.

4. COMSOL multiphysics modelling

The MEMS meander beam and rectangular beam accelerometers have been simulated in COMSOL by utilizing the Solid Mechanics (SM) physics. The properties of Silicon have been manually defined as mentioned in Table 1. In order to simplify the meshing procedure, a composite domain has been generated including beams and the proof mass. In the SM physics, a body load normal to the proof mass has been applied considering an acceleration of 0.01 ms^{-2} so as to emulate low accelerations. The damping due to air in the system is simulated using thin-film damping. An attractive feature of this boundary condition is that encapsulating plates need not be geometrically defined. The damping is simulated mathematically considering the gap height derived in SPICE and the modified Reynold's equation. The wall and base distances are defined by solving an initial step for the stationary study. The direction of normal vectors assist in defining boundaries as well as wall and plate distances and can be viewed during post processing. This step is important since incorrect boundary referencing can lead to instabilities in the solver and incorrect results. A gap height is set as 9.66 µm and the additional wall displacement equal to

that of the proof mass. The response of the accelerometers has been characterized by 3 studies:

1) *Eigenfrequency*: The higher order modes as well as the resonance mode of the accelerometers are evaluated in this study which provide deeper insights into the parasitic tilting of the accelerometers.
2) *Time Dependent*: This study is performed on the meander beam sensor with a parametric sweep on the squeeze-film gap height in order to visualize the damping of the proof mass via transient displacement. The steps taken by the solver have been defined manually with a time step of 0.00001 alongside linear prediction.
3) *Stationary:* This study is performed on the meander beam sensor with an auxiliary sweep on the body load. This is performed to simulate the differences arising between the COMSOL and SPICE derived displacement of the proof mass as the force increases.

The distribution of mesh elements at the interface of the beams with the proof mass has been increased to 15 elements with an element ratio of 2 in order to improve accuracy. The results of the studies are discussed in section 5.

5. Simulation results

Eigenfrequencies: A total of 4 eigen-modes have been simulated, each corresponding to one resonance movement (no rotation about sensor axes) and three parasitic modes which comprise of tilts and rotations around the axes of the sensor. This is highlighted in Fig. 7 wherein Fig. 7a is representative of pure translational movement on the application of force and Fig. 7b-d indicate the rotational moments around the x-y axes of the sensor. The resonance frequency derived in COMSOL (= 1453.9 Hz) is in close agreement with the SPICE derived results (= 1575 Hz). The difference between the values can be attributed to the assumptions used during the analytical modeling. The mass of the structure is higher than the analytically derived value due to the finite mass of the beams as well as the presence of parasitic tilts in the device. The combination of these factors leads to a drop in the resonance frequency computed in COMSOL. Additionally, the eigen-modes of a rectangular beam accelerometer have been simulated as shown in Fig. 7e-h and the results summarized in Table 2

Table 2. Eigen-modes of meander bean and rectangular beam accelerometer.

	Meander Beam	Rectangular Beam
Resonance Frequency (Hz)	1453.9	1118.2
Parasitic Frequencies (Hz)	2044, 2044.8, 29866	1024.8, 1031.1, 24624

As observed in Table 2, the resonance frequency of the rectangular beam sensor is lower than that of the meander beam. Furthermore, the higher order modes occur at frequencies closer to the resonance mode in rectangular beam design, a property which is undesirable during sensor design due to lowering of operation bandwidth. The frequency range between the resonance and parasitic modes have dropped by 80% in rectangular beams. This leads to an increase in the off-axis sensitivity of the proof mass. Placement of the beams at the center could further alleviate the moments about the x and y axes leading to a drop in resonance frequency which leads to a higher effective damping. To validate this reasoning, the distance of the meander beams from the edge of the proof mass, L_1 (in μm), has been increased successively reducing the gap between each beam and moving them closer to the center of the proof mass. The drop in the vertical steady-state displacement due to the beam shift is shown in Fig. 8 which confirms our hypothesis. This drop is lower than 0.3% which indicates the robustness of meander beams.

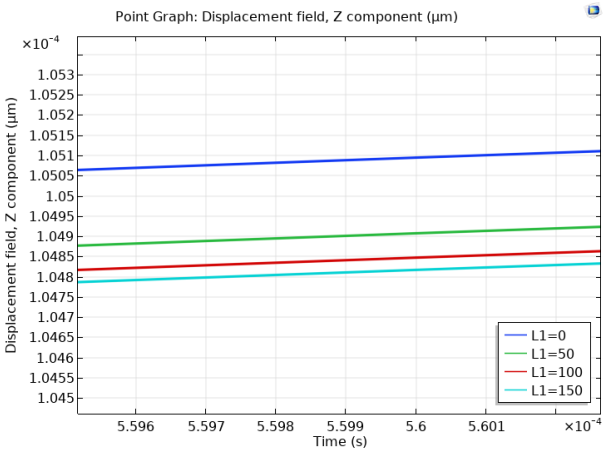

Figure 8. Vertical displacement of proof mass vs beam distance (L_1) from the edge of the proof mass. All beam distance values are in μm.

Transient response: The time-dependent response of the sensor is analyzed for varying gap heights (H) and by extension damping ratios. The resulting curves excellently show the damping of the sensor validating the initial conditions of thin-film damping as shown in Fig. 9. The drop in resonance frequency in COMSOL leads to an increase in the damping ratio of the system. At a gap height of 9.66 μm, a critically flat

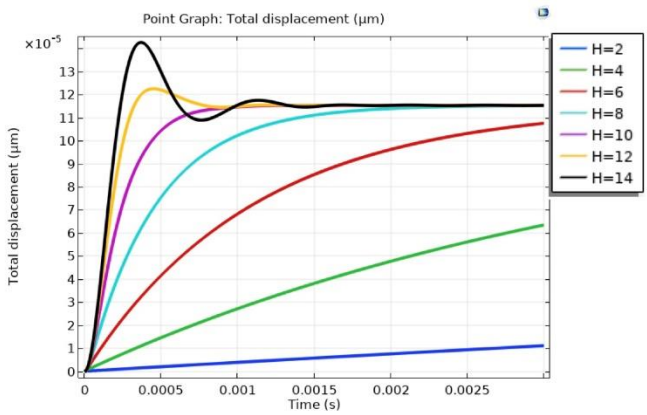

Figure 9. Transient response of accelerometer with squeeze film damping for varying encapsulation gap height, H (μm).

response is observed wherein $\zeta \approx 1$ while in LTspice the observed damping ratio was evaluated as 0.707 for the same gap height. On substituting the COMSOL derived resonance frequency in Eq. 5, a damping ratio of 1.1 is calculated. This highlights the robust compatibility between the COMSOL and SPICE frameworks.

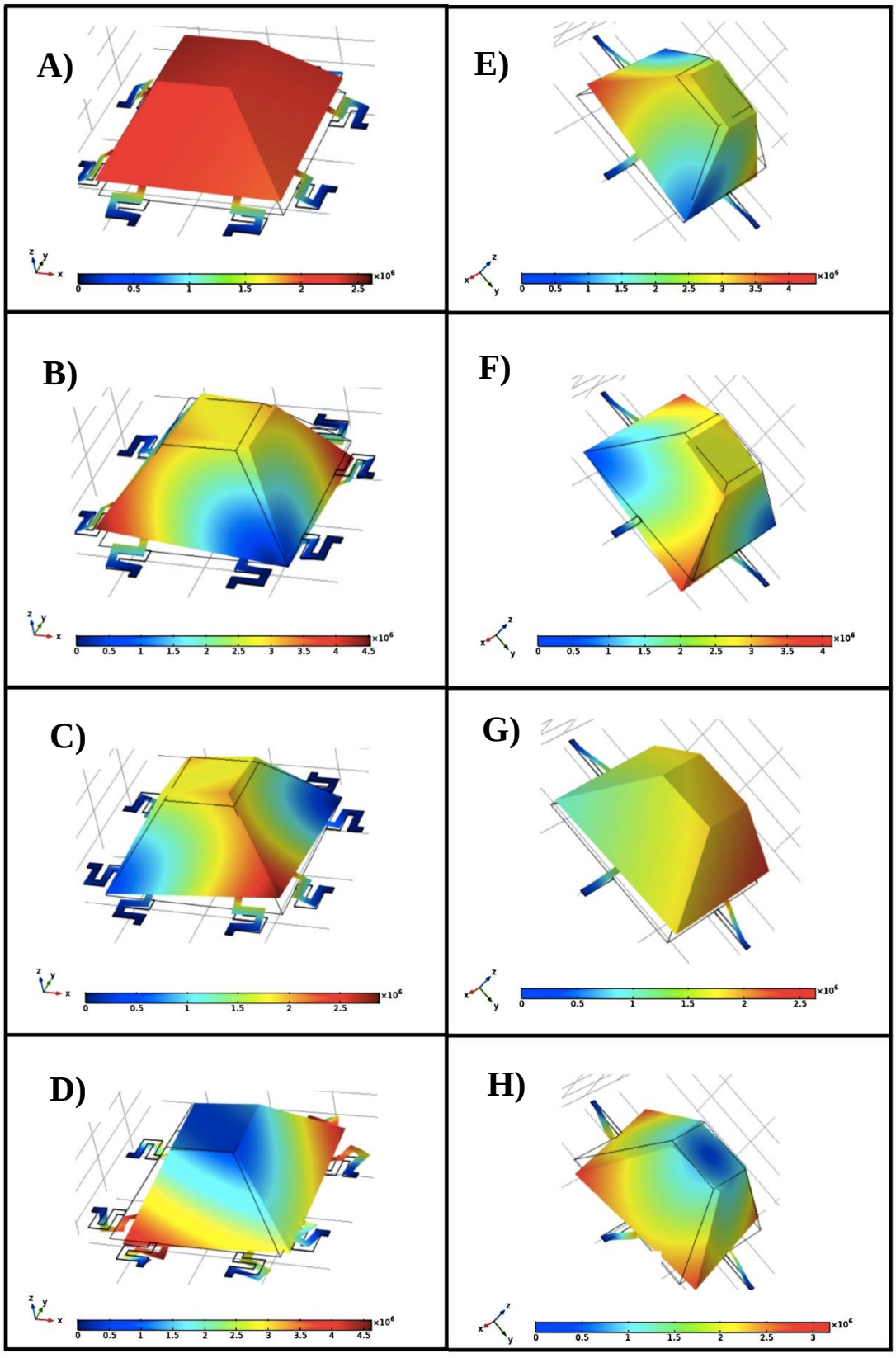

Figure 7. Surface displacement of meander beam (a-d) and rectangular beam (e-h) accelerometers. a) First mode (translational) b) Second mode (rotational) c) Third mode (rotational) d) Fourth mode (Beam twist) e) First mode (rotational) b) Second mode (rotational) c) Third mode (semi-translational) d) Fourth mode (Beam twist). Data set edges (initial sensor position) are shown in black.

The transition of the damping characteristics from under damped to over damped with reduction in gap height can be clearly observed in Fig. 9. At lower gap heights, the pressure caused on the top and bottom surfaces of the sensor due to air flow increases thereby increasing the damping ratio. As the compressibility of the squeeze-film increases, the duration required for the sensor to reach a stable response increases and hence a critically damped response is preferred experimentally.

Stationary study: The fundamental equations associated with analytical derivations of accelerometer response utilize the base assumption that displacement in the beams can be approximated using small deformation theory. As the force on the proof mass increases, lateral stresses arise in the beams and the constitutive relations should be redefined taking into consideration that the tangents to the beams can no longer be simplified ($\tan\theta \ncong \theta$). The difference between the LTspice and COSMOL derived proof mass displacement is shown in Fig. 10.

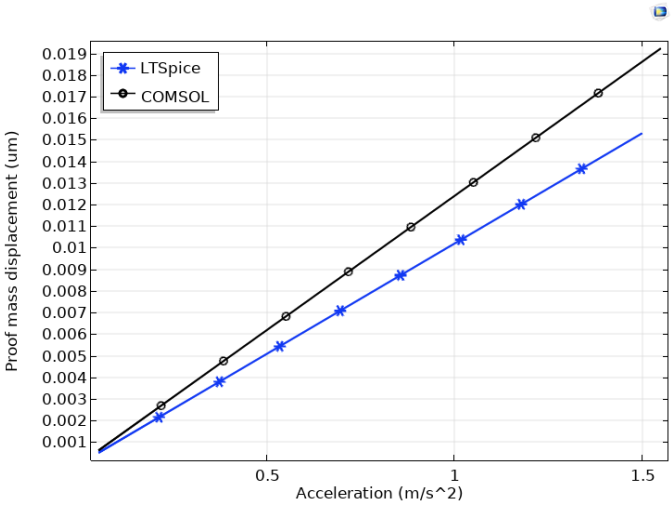

Figure 10. Proof mass displacement vs acceleration of the meander beam sensor. The resulting response derived in LTspice and COMSOL begin to diverge as acceleration increases.

The error between the two models increases at a rate of 0.018 $\mu m/ms^{-2}$ and occurs due to the presence of deformation gradients occurring in the beam at higher deflections. In order to circumvent this, new analytical models are required which take into account the stresses which arise in the beams at higher deflections.

6. Conclusions

In this paper the response of a meander beam accelerometer was simulated in LTspice and COMSOL. The three dimensional model was setup in COMSOL in order to emulate the response of the accelerometer across all three axes due to parasitic components. The variation of proof mass displacement was derived in COMSOL as well as SPICE. The analytical equations reflect the efficiency of coupling between the electrical and mechanical domains via the derivation of damping factor for various cases of squeeze film damping. The co-ordinates of the beams along the edges of the proof mass as well as the number of beams are significant design parameters due to their contributions to the development of parasitic moments. In order to improve the efficiency of the analytical model, large deflection theory must be utilized.
On account of the low size and mass of the sensor, it can be fabricated using standard CMOS processing with electrostatic feedback capabilities. On packaging, the sensors can be primarily utilized in medical devices and instruments due to their high sensitivity.

Acknowledgements

The author would like to thank Dr. Andre Bossche for his valuable inputs through-out the project.

References

[1] Z. Mohammed, I. (Abe) M. Elfadel, and M. Rasras, “Monolithic multi degree of freedom (MDoF) capacitive MEMS accelerometers”, *Micromachines*, vol. 9, no. 11. MDPI AG, 16-Nov-2018.

[2] J. Tian, W. Yang, Z. Peng, T. Tang, and Z. Li,” Application of MEMS accelerometers and gyroscopes in fast steering mirror control systems”, *Sensors (Switzerland)*, vol. 16, no. 4, Mar. 2016.

[3] W. Y. Lin, V. K. Verma, M. Y. Lee, and C. S. Lai, “Activity monitoring with a wrist-worn, accelerometer-based device”, *Micromachines*, vol. 9, no. 9, 2018.

[4] A. Utz, C. Walk, A. Stanitzki, M. Mokhtari, M. Kraft, and R. Kokozinski, “A high precision MEMS based capacitive accelerometer for seismic measurements,” in Proceedings of IEEE Sensors, 2017, vol. 2017, December, pp. 1–3.

[5] S. Biswas and A. K. Gogoi, “Design and simulation of piezoresistive MEMS accelerometer for the detection of pathological tremor”, in Conference Proceedings-IEEE SOUTHEASTCON, 2014.

[6] K. Rao, X. Wei, S. Zhang et al., “A MEMS Micro-g Capacitive Accelerometer Based on Through-Silicon-Wafer-Etching Process, *Micromachines*, vol. 10, no. 6, p. 380, Jun. 2019.

[7] G. K. Fedder, “Simulation of Microelectromechanical Systems”, Ph.D. Thesis, University of California at Berkeley, 1994.

[8] H. V. Allen, S. C. Terry, and D. W. De Bruin, “Accelerometer systems with self-testable features” *Sensors and Actuators*, vol. 20, no. 1-2, pp. 153-161, Nov. 1989.